

Net-Zero Integrated Sensing and Communication in Backscatter Systems

Yu Zhang, Tongyang Xu, Christos Masouros[†], and Zhu Han[‡]

School of Engineering, Newcastle University, Newcastle upon Tyne NE1 7RU, United Kingdom

[†]Department of Electronic and Electrical Engineering, University College London, London WC1E 6BT, United Kingdom

[‡]Department of Electrical and Computer Engineering, University of Houston, TX 77004, USA

Email: yu.zhang@newcastle.ac.uk, tongyang.xu@newcastle.ac.uk, c.masouros@ucl.ac.uk, zhan2@uh.edu

Abstract—Future wireless networks targeted for improving spectral and energy efficiency, are expected to simultaneously provide sensing functionality and support low-power communications. This paper proposes a novel net-zero integrated sensing and communication (ISAC) model for backscatter systems, including an access point (AP), a net-zero device, and a user receiver. We fully utilize the backscatter mechanism for sensing and communication without additional power consumption and signal processing in the hardware device, which reduces the system complexity and makes it feasible for practical applications. To further optimize the system performance, we design a novel signal frame structure for the ISAC model that effectively mitigates communication interference at the transmitter, tag, and receiver. Additionally, we employ distributed antennas for sensing which can be placed flexibly to capture a wider range of signals from diverse angles and distances, thereby improving the accuracy of sensing. We derive theoretical expressions for the symbol error rate (SER) and tag’s location detection probability, and provide a detailed analysis of how the system parameters, such as transmit power and tag’s reflection coefficient, affect the system performance.

Index Terms—ISAC, net-zero, backscatter communication, localization, distributed antenna.

I. INTRODUCTION

Integrated sensing and communication (ISAC) has emerged as an important technology in the evolution towards 6G communications. The key concept of ISAC is integrating sensing and communication functions into one device, which improves the spectrum and energy efficiency and reduces the hardware cost [1]. This dual functionality makes ISAC beneficial in applications such as autonomous vehicles, smart cities, and the Internet of Things (IoT), where real-time sensing and communication are essential. ISAC has gained significant research interest in areas, such as waveform design, and trade-off analysis [2].

With the popularity of sustainable development and energy-saving concepts, net-zero devices have attracted much attention [3]. Unlike traditional devices that require batteries, net-zero devices operate without a battery. Instead, they harvest energy from the surrounding environment, particularly from ambient radio frequency (RF) signals. The working mechanism of net-zero devices is backscattering, where they reflect incoming RF signals from nearby transmitters, such as TV towers, mobile phones, or WiFi routers, to convey information

[4]. This backscatter mechanism allows the devices to operate at extremely low power levels, often in the microwatt range.

ISAC technology is particularly well-suited for net-zero devices since they can perform sensing and communication tasks simultaneously using the same RF signals. The net-zero devices can provide sensing information while simultaneously transmitting information data to a specific receiver. However, there is limited research conducted on backscatter enabled ISAC system. In [5], the authors introduce an ISAC framework including a base station (BS), a tag, and a user, which derives the communication rate of the user and the tag, as well as the sensing rate at the BS. Similar to conventional ISAC systems, this model still requires optimization of the power allocation factor to balance the trade-off between communication and sensing. Another study involves ISAC for reconfigurable intelligent surface (RIS)-assisted backscatter communication [6], where the BS simultaneously detects backscattered signals from the RIS-assisted IoT devices and senses targets based on the echo signals. However, this study doesn’t consider the interference between different IoT devices.

The above-mentioned literature on ISAC system design mainly focuses on the joint waveform design for sensing and communication. These studies do not fully leverage the potential of backscattered signals from net-zero devices, which can be used for both communication and sensing. In our study, we utilize an access point (AP), such as Wi-Fi, to send signals to net-zero devices. The backscattered signal from the net-zero device can be used for sensing purposes, such as localization. This approach eliminates the need for additional waveform designs for sensing and communication, thereby reducing system complexity and enhancing energy efficiency.

II. SYSTEM MODEL

In Fig. 1, the proposed net-zero ISAC system model consists of an AP, a passive tag, and a receiver. The AP is equipped with a single transmit antenna and N distributed receive antennas. The advantage of using distributed antennas is that they can be placed across different indoor locations. This placement flexibility enables the AP to capture a wider range of signals from diverse angles and distances, thereby improving the accuracy of sensing. Both the transmitter and receiver antennas have omnidirectional radiation patterns.

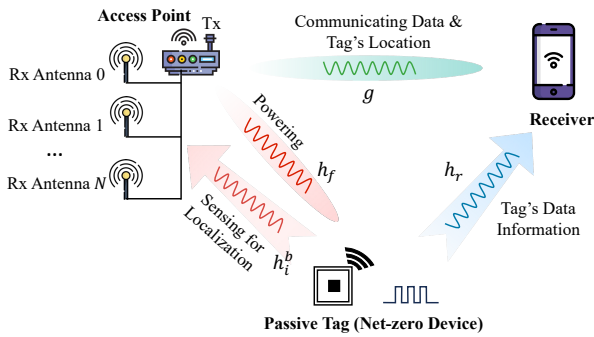


Fig. 1. System model of the ISAC for net-zero devices.

The AP sends a query signal to activate the passive tag. Subsequently, the tag modulates its data onto the incident RF signals and backscatters them toward both the AP and the receiver. The AP leverages the received backscattering signals across all N distributed receive antennas for sensing. In this paper, we focus on using the sensing information for localization. The advantage of localization sensing lies in three aspects. Firstly, the sensing results assist in beamforming for powering the tag. Initially, an omnidirectional beam is used to both power the tag and sense its location. Once the location is determined, a directional beam is employed to enhance power delivery to the tag, simultaneously improving communication performance. Secondly, in indoor environments, localization can track user movements and detect intrusions. Thirdly, in underground spaces where GPS signals are unavailable, localization proves effective.

Since the proposed ISAC model is based on existing hardware, it does not require additional hardware costs. The signal processing for localization is conducted at the AP. The receiver, a low-cost device, captures both the signal from the AP and the backscattered signals from the tag. These backscattered signals contain the tag's data, such as temperature and humidity, which the receiver demodulates. Simultaneously, the signals from the AP provide communication services and the location information of the tag.

A. Frame Structure Design

To reduce the complexity of the proposed system, we design a novel frame structure of the ISAC model that effectively mitigates interference at the transmitter, tag, and receiver. As illustrated in Fig. 2, the frame structure contains a downlink (DL) time slot and an uplink (UL) time slot. During the DL time slot, the AP sends signals to power the tag while simultaneously transmitting communication data to the receiver. In contrast, during the UL time slot, the AP is configured to only receive signals from the tag without transmitting any signals itself. Consequently, during the UL time slot of the AP, the receiver only captures the backscattered signals from the tag, free from interference caused by transmissions from the AP. This strategic design of the frame structure effectively achieves interference elimination, reducing system complexity.

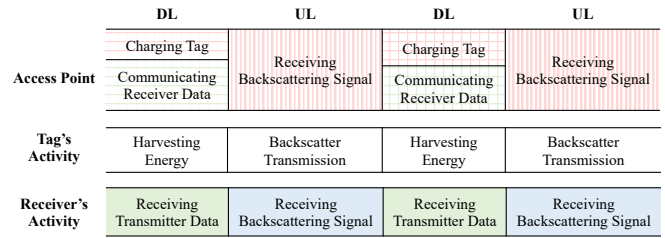


Fig. 2. Frame structure of AP corresponding to the activities of the passive tag and receiver.

B. Backscatter Modulation

As a net-zero device, the passive tag doesn't have an internal battery to supply the power. Instead, it harvests the energy from the incident RF signals, modulating its own data onto the RF carrier and reflecting it back to the AP. The modulation of a tag is achieved by adjusting the reflection coefficient to realize different modulation schemes. As shown in Fig. 3(a), to create an M -ary modulation, the tag utilizes M load impedance values to generate M different reflection coefficients, with the m -th coefficient defined as [4]

$$\Gamma^{(m)} = \frac{Z_L^{(m)} - Z_a}{Z_L^{(m)} + Z_a} = \Gamma_R^{(m)} + j\Gamma_I^{(m)}, \quad (1)$$

where $Z_L = R_L + jX_L$ is the complex load impedance and $Z_a = R_a + jX_a$ is the complex antenna impedance. The real components, R_L and R_a are the load and antenna resistances, respectively, while the imaginary components, X_L and X_a are the load and antenna reactances, respectively. In (1), the reflection coefficient Γ is a complex value comprising the real part Γ_R and imaginary part Γ_I . This complex nature allows the modulation of both the amplitude and phase of the reflected signals by adjusting the load impedance Z_L . As shown in Fig. 3(a), the incident RF signals captured by the passive tag's antenna, $|\Gamma|^2 P_{in}$ of RF power is backscattered while $(1 - |\Gamma|^2) P_{in}$ is absorbed in the load.

The Smith chart is an effective tool for mapping load impedance to the reflection coefficient. To utilize the Smith chart, we need to first normalize the load impedance, i.e., $Z'_L = Z_L/Z_a$, and then Γ is calculated as $\Gamma = \frac{Z'_L - 1}{Z'_L + 1}$. As shown in Fig. 3(b), the Smith chart consists of two types of circles: the green circle represents the real part and the pink circle represents the imaginary part of Z'_L . For example, given $Z_a = 50\Omega$ and $Z_L = 100 + j50\Omega$, after normalizing, Z'_L becomes $2 + j$. Plot the intersection point of the resistance circle with value 2 and the reactance circle with value 1j, i.e., point P in Fig. 3(b). The projections on the horizontal and vertical axes of the Cartesian coordinates are the real part and the imaginary part of the reflection coefficient, respectively. Here we get point P corresponding to the reflection coefficient $\Gamma = 0.4 + 0.2j$. For example, by adjusting the value of $Z_L^{(m)}$, we can easily achieve 4-QAM modulation, as demonstrated by the four blue star points shown in Fig. 3(b).

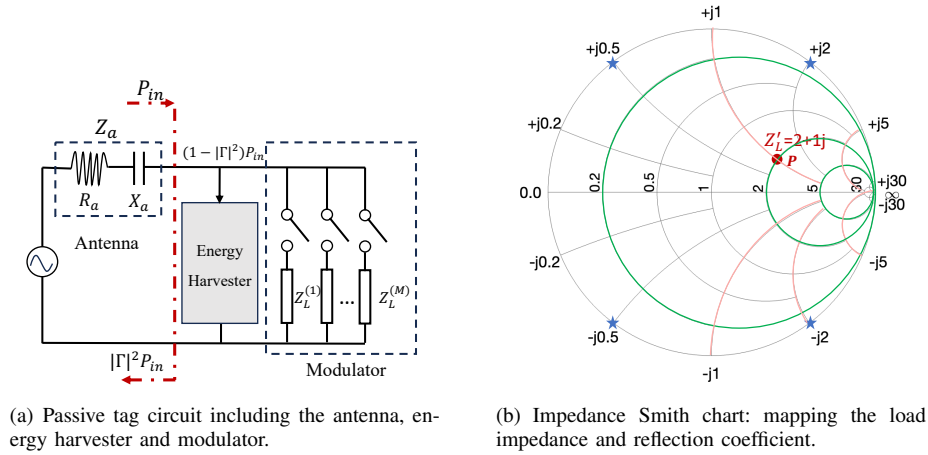


Fig. 3. The passive tag circuit and the Smith chart.

C. AP Sensing Model

The received signal strength (RSS) at AP which is backscattered from the tag can be used as sensing information for localization. RSS measurements can be easily obtained from the received antennas without requiring additional hardware. Moreover, this approach is cost-effective and low-power, making it particularly suitable for net-zero device localization. The fundamental principle of the RSS-based localization method involves computing the distance between the transmitter and receiver by comparing the transmit and receive power. The total received power at the i -th antenna is given by [7]

$$P_i^R = \chi P_s G_{tag} G_T G_R^i L(d_f) L(d_i^b) |h_f h_i^b \Gamma|^2, \quad (2)$$

where χ is the polarization loss factor, P_s is the transmit power of AP, G_{tag} is the antenna gain of the tag, G_T and G_R^i are the antenna gains of transmit antenna and i -th receive antenna of AP, respectively. The distance between transmit antenna and i -th receive antenna of AP to the tag are denoted as d_f and d_i^b , respectively. $L(\cdot)$ is the channel path loss model, given by [8]

$$L(d_k) = \left(\frac{d_k}{d_0}\right)^{-\eta}, \quad (3)$$

where η is the path loss exponent and d_0 is the reference distance.

It is important to note that the received backscattered power must exceed the sensitivity threshold of the receiving antennas. Under this condition, the tag's location becomes detectable. For a given tag, if it is captured by receiving antenna i , we denote the *antenna capture indicator* L_i as 1, where it is defined as: [9]

$$L_i = \begin{cases} 1, & P_i^R \geq P_{th}, \\ 0, & \text{otherwise,} \end{cases} \quad (4)$$

where P_{th} is the sensitivity threshold. In the RSS-based trilateration localization method, determining a tag's location requires a minimum of three distinct RSS measurements.

Consequently, the probability of successfully localizing a tag is defined by the following:

$$P_{Loc} = \Pr \left\{ \sum_{i=1}^N L_i \geq 3 \right\}. \quad (5)$$

III. PERFORMANCE ANALYSIS

In this section, we will give the performance analysis of the proposed ISAC for net-zero devices, which is focused on how the transmit power of AP and reflection coefficient of tag affect the tag's location detection probability and symbol error rate (SER). Specifically, we will present a detailed derivation of the tag's location detection probability and theoretical upper bound of SER under different modulation schemes. This analysis aims to provide insights on how to adjust the transmit power of AP, the position of distributed antennas and reflection coefficient of tag to improve the system performance.

A. Localization Performance

The RSS-based localization method relies on the strength of the received signal from different positions, which is significantly influenced by multipath propagation. Therefore, choosing an appropriate channel fading model is very important. In this paper, we focus on the Rician and Rayleigh fading models to represent indoor signal propagation. The Rician model is usually for scenarios where there is a dominant line-of-sight (LOS) component along with numerous indirect paths. The Rayleigh model is used in environments where there is no dominant line-of-sight path, and the signal is scattered in multiple directions. If we consider h_f and h_i^b are independent Rician random variables, then the probability density function (PDF) of $h_i = h_f h_i^b$ is expressed as [10]

$$p_{h_i}(x) = \frac{x \exp[-(K_f + K_b^i)]}{\sigma_f^2 \sigma_b^2} \sum_{m=0}^{\infty} \sum_{n=0}^{\infty} \frac{1}{(m!n!)^2} \left(\frac{x K_f}{2\sigma_f^2}\right)^m \times \left(\frac{x K_b^i}{2\sigma_b^2}\right)^n \left(\frac{\sigma_f}{\sigma_b}\right)^{m-n} \mathbf{K}_{m-n}\left(\frac{x}{\sigma_f \sigma_b}\right), x \geq 0, \quad (6)$$

where $\mathbf{K}(\cdot)$ is the modified Bessel function of the second kind, $\{K_f, \sigma_f\}$ and $\{K_b^i, \sigma_b\}$ are the Rician shape parameters for both the forward and backscatter links, respectively, where K_f and K_b^i is defined as the ratio of the power contributions by line-of-sight (LoS) path to the remaining multipath. For the special case of $K_f = K_b^i = 0$, the envelope of h_f and h_b^i become two independent Rayleigh random variables.

To derive the localization probability in (5), we can use the binomial distribution to calculate the probability of at least three out of I receive antennas' RSS measurements exceeding the threshold P_{th} . Let's denote $X = \sum_{i=1}^N L_i$, and then (5) can be rewritten as

$$\begin{aligned} P_{Loc} &= 1 - \Pr\{X \leq 3\} \\ &= 1 - \Pr\{X = 0\} - \Pr\{X = 1\} - \Pr\{X = 2\}, \end{aligned} \quad (7)$$

where $\Pr\{X = k\} = \sum_{i=1}^k \left(\prod_{j=1, j \neq i}^k p_j \right) (1-p_i)$ and p_i is given as follows

$$\begin{aligned} p_i &= \Pr\{P_i^R \geq P_{th}\} \\ &= \Pr\left\{ \chi P_s G_{tag} G_T G_R^i L(d_f) L(d_i^b) |h_f h_i^b \Gamma|^2 \geq P_{th} \right\}, \end{aligned} \quad (8)$$

where p_i represents the probability that i -th receive antenna of AP can detect the location of tag. Let's denote $\zeta = \chi P_s |G_{tag} G_T G_R^i L(d_f) L(d_i^b) \Gamma|^2$, then (8) can be written as

$$\begin{aligned} p_i &= 1 - \int_0^{\sqrt{P_{th}/\zeta}} p_{h_i}(x) dx \\ &= 1 - \frac{A}{2} \sum_{m=0}^{\infty} \sum_{n=0}^{\infty} \int_0^1 \left(\frac{P_{th}}{\zeta} \right)^{\frac{m+n+2}{2}} x^{\frac{i+1}{2}} \mathbf{K}_{m-n} \left(\sqrt{\frac{P_{th} x}{\zeta \sigma_f^2 \sigma_b^2}} \right) dx, \end{aligned} \quad (9)$$

where $A = \frac{\exp[-(K_f + K_b^i)]}{\sigma_f^2 \sigma_b^2 (m!n!)^2} \left(\frac{K_f}{2\sigma_f^2} \right)^m \left(\frac{K_b^i}{2\sigma_b^2} \right)^n \left(\frac{\sigma_f}{\sigma_b} \right)^{m-n}$. According to the Eq. (6.592.2) in [11], we can derive the tag location detection probability of antenna i for the Rician fading scenario, as follows:

$$\begin{aligned} p_i &= 1 - \frac{A}{4} \sum_{m=0}^{\infty} \sum_{n=0}^{\infty} (2\sigma_f^2 \sigma_b^2)^{m-n} \left(\frac{P_{th}}{\zeta} \right)^{n+1} \\ &\quad \times G_{1,3}^{2,1} \left(\frac{P_{th}}{4\zeta \sigma_f^2 \sigma_b^2} \left|_{m-n, 0, -n-1} \right. \right)^{-m}, \end{aligned} \quad (10)$$

where $G_{p,q}^{m,n}$ is the Meijer G-function, as defined in [11, P1032, Eq. (9.301)]. From (10), we note that the derived tag location detection probability involves two infinite summation series, making it difficult to determine how the parameters affect system performance. To simplify the analysis and gain insights on parameter effects, we consider the scenario where $K_f = K_b^i = 0$ in (10), corresponding to Rayleigh fading. The tag location detection probability under Rayleigh fading is then given by:

$$p_i = 1 - \frac{P_{th}}{4\zeta \sigma_f^2 \sigma_b^2} G_{1,3}^{2,1} \left(\frac{P_{th}}{4\zeta \sigma_f^2 \sigma_b^2} \left|_{0,0,-1} \right. \right)^0. \quad (11)$$

The derived p_i under Rayleigh fading is mathematically less complex, involving only a single Meijer G-function. By examining the monotonicity of the function, we can directly obtain how parameters influence the system performance.

Theorem 1. $f(x) = 1 - x G_{1,3}^{2,1} \left(x \left|_{0,0,-1} \right. \right)^0$ is a monotonically decreasing when $x > 0$.

Proof. According to [11, Eq. (9.31.3)], we can derive the first derivative of $f(x)$ is

$$\begin{aligned} \frac{df(x)}{dx} &= -G_{1,3}^{2,1} \left(x \left|_{0,0,-1} \right. \right)^0 - x \frac{dG_{1,3}^{2,1} \left(x \left|_{0,0,-1} \right. \right)^0}{dx} \\ &= -G_{1,3}^{2,1} \left(x \left|_{0,0,-1} \right. \right)^{-1} = -2K_0(2\sqrt{x}) < 0. \end{aligned} \quad (12)$$

Since the first derivative of $f(x) < 0$, $f(x)$ is a monotonically decreasing function. Therefore, the Theorem 1 is proved. \square

Based on Theorem 1, we can find that the tag's location detection probability will be increased with the transmit power P_s and reflection coefficient $|\Gamma|^2$ increase, but decreases as the distance between receive antenna i and tag increases.

B. SER Performance

We consider the forward link channel h_f and backscatter link channel of receiver h_r both as Rayleigh fading, then the instantaneous defined SNR is

$$\gamma = \frac{\chi P_s G_{tag} G_T G_R L(d_f) L(d_r) |h_f h_r \Gamma|^2}{N_0} = \Xi |h_f h_r|^2, \quad (13)$$

where G_R is the antenna gain of the receiver, d_r is the distance between the receiver and tag, N_0 is the noise power spectral density, and $\Xi = \chi P_s G_{tag} G_T G_R L(d_f) L(d_r) |\Gamma|^2 / N_0$.

We utilize the moment generation function (MGF)-based method to derive the SER. For the M -PSK and M -QAM modulation, the SER can be written as follows [12]

$$P_{\text{MPSK}} = \frac{1}{\pi} \int_0^{\pi - \frac{\pi}{M}} \mathcal{M}_\gamma \left(\frac{g_{\text{MPSK}}}{\sin^2 \theta} \right) d\theta, \quad (14)$$

$$\begin{aligned} P_{\text{MQAM}} &= \frac{4}{\pi} \left(1 - \frac{1}{\sqrt{M}} \right) \int_0^{\frac{\pi}{2}} \mathcal{M}_\gamma \left(\frac{g_{\text{MQAM}}}{\sin^2 \theta} \right) d\theta \\ &\quad - \frac{4}{\pi} \left(1 - \frac{1}{\sqrt{M}} \right)^2 \int_0^{\frac{\pi}{4}} \mathcal{M}_\gamma \left(\frac{g_{\text{MQAM}}}{\sin^2 \theta} \right) d\theta, \end{aligned}$$

where $g_{\text{MPSK}} = \sin^2(\pi/M)$ and $g_{\text{MQAM}} = \frac{3}{2(M-1)}$ are the M -PSK and M -QAM constellation constant, respectively. $\mathcal{M}_\gamma(\cdot)$ is the MGF of γ , defined as

$$\mathcal{M}_\gamma(s) = \mathbb{E}\{e^{-s\gamma}\} = \int_0^\infty e^{-s\gamma} f(\gamma) d\gamma, \quad (15)$$

where $f(\gamma)$ is the PDF of γ . Let $X_1 = |h_f|^2$ and $X_2 = |h_r|^2$, if h_f and h_r are both Rayleigh fading, we have X_1 and X_2 are both Gamma distribution, with PDF

$$f_{X_1}(x_1) = \frac{x_1}{\Omega_f^2} \exp\left(-\frac{x_1}{\Omega_f}\right), \quad (16)$$

$$f_{X_2}(x_2) = \frac{x_2}{\Omega_r^2} \exp\left(-\frac{x_2}{\Omega_r}\right), \quad (17)$$

where Ω_f and Ω_r are Rayleigh fading parameters of the forward link and backscatter link, respectively. The MGF of $X = X_1 X_2$ is defined as

$$\mathcal{M}_X(s) = \int_0^\infty \int_0^\infty e^{-x_1 x_2 s} f(x_1, x_2) dx_1 dx_2. \quad (18)$$

Substituting (16) and (17) into (18), we can obtain [12]

$$\mathcal{M}_X(s) = \left(\frac{1}{\Omega_f \Omega_r s}\right)^2 \Psi\left(2, 1, \frac{1}{\Omega_f \Omega_r s}\right), \quad (19)$$

where $\Psi(a, b; z)$ is the Tricomi confluent hypergeometric function also denoted by $U(a, b, z)$. Based on $\gamma = \Xi X$, we have

$$\mathcal{M}_\gamma(s) = \mathcal{M}_X(\Xi s) = \left(\frac{1}{\Omega_f \Omega_r \Xi s}\right)^2 \Psi\left(2, 1, \frac{1}{\Omega_f \Omega_r \Xi s}\right). \quad (20)$$

Substituting (20) into (14) and (15), the average SER for M -PSK and M -QAM can be derived. However, the derivation contains the hypergeometric function, making the closed form of the SER difficult to obtain. Let $\theta = \pi/2$, we can derive the Chernoff bound as

$$P_{\text{MPSK}} \leq \left(1 - \frac{1}{M}\right) \left(\frac{1}{g'_{\text{MPSK}}}\right)^2 \Psi\left(2, 1, \frac{1}{g'_{\text{MPSK}}}\right), \quad (21)$$

$$P_{\text{MQAM}} \leq \left(1 - \frac{1}{M}\right) \left(\frac{1}{g'_{\text{MQAM}}}\right)^2 \Psi\left(2, 1, \frac{1}{g'_{\text{MQAM}}}\right), \quad (22)$$

where $g'_{\text{MPSK}} = \sin^2(\pi/M) \Omega_f \Omega_r \Xi$, $g'_{\text{MQAM}} = \frac{3\Omega_f \Omega_r \Xi}{2(M-1)}$. The monotonicity of the function is hard to obtain directly from the first derivative of (21) and (22) due to the hypergeometric function $\Psi(a, b; z)$. We will use the numerical methods to evaluate the performance in the next section.

IV. NUMERICAL RESULTS

In this section, we present the simulation results of the tag's location detection probability and SER. On one hand, the numerical results can verify the accuracy of the theoretical analysis. On the other hand, they can provide an intuitive evaluation when the theoretical derivative is too complex or not feasible to compute. All the simulation parameter settings are shown in Table I. We use MATLAB to generate the Rician and Rayleigh simulations, with the number of simulations set at 10^6 . The Meijer G-function and Tricomi confluent hypergeometric function are also available in MATLAB.

Fig. 4 illustrates the performance of tag's location detection probability under different fading conditions. The performance under Rayleigh fading is worse than that under Rician fading.

TABLE I
PARAMETERS VALUES

Parameter	Description	Value
χ	Polarization loss factor	0.5
G_{tag}	Tag's antenna gain	0dBi
G_T	AP's transmit antenna gain	0dBi
G_R^i	AP's receive antenna gain	0dBi
G_R	Receiver's antenna gain	0dBi
$ \Gamma ^2$	Reflection coefficient	[0, 1]
η	Path loss factor	1.8
P_{th}	Sensitivity threshold	-75dBm
σ_f	Forward link Rician parameter	1
σ_b	Backscatter link Rician parameter	1

This is because Rayleigh fading lacks a line-of-sight (LOS) component and is more severely affected by multipath propagation. If the theoretical analysis in Rician fading is hard to obtain, using Rayleigh fading as an alternative can provide a more conservative benchmark for system performance. Moreover, increasing the Rician fading parameters K_f and K_b improves the performance. It is interesting to note that the performance remains consistent whether $K_f = 1, K_b = 0$ or $K_f = 0, K_b = 1$, which suggests the impact of these parameters on the cascaded channel fading is symmetric.

In Fig. 5, we demonstrate how the distance between the tag and the receive antennas affects the tag's location detection probability. As we can see, when the receive antenna distance is 5m away from the tag, the detection probability is about 30% with $P_s = 1W$. The detection probability significantly increases to 90% when the distance is reduced to 2m. Moreover, the probability that at least 3 antennas can detect the tag's location is about 50%. These results indicate that achieving a detection probability of at least 50% requires that the distance between the tag and any receive antenna cannot exceed 5m. We also verified the independence of each receive antenna during simulations. The correlation heatmap in Fig. 6 shows the low correlation between different antennas, which supports the reliability of the simulation results.

In Fig. 7, we analyze the effects of increasing the reflection coefficient on the tag's location detection probability and SER. The tag's location detection probability increases as the reflection coefficient increases, while the SER decreases. However, the variations in SER across different reflection coefficients are relatively minor, which indicates that the choice of the reflection coefficient is flexible without significantly compromising the quality of communication. Furthermore, the SER has better performance under QAM modulation than that of PSK.

V. CONCLUSION

In this paper, we propose a novel net-zero ISAC model utilizing the backscatter properties of net-zero devices, which

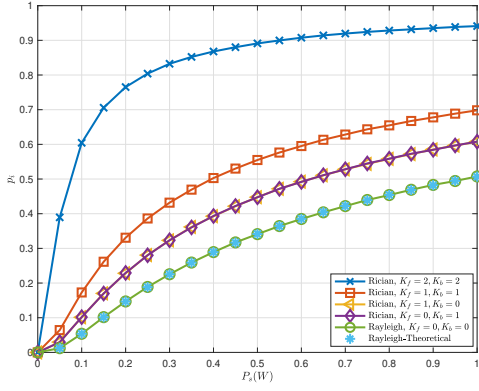


Fig. 4. Tag's location detection probability of i -th receive antenna p_i versus transmit power P_s under different fading channels.

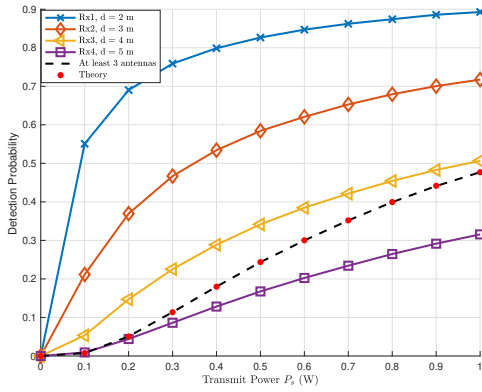


Fig. 5. Tag's location detection probability for different receive antennas.

simplifies the system design without additional power consumption and hardware. Our proposed frame structure design effectively mitigates interference at the transmitter, tag, and receiver. Through theoretical derivation of the tag's location detection probability and SER, we obtain valuable insights on parameter adjustments for improving sensing and communication performance. Furthermore, we demonstrate the flexibility of choosing the reflection coefficient to improve tag's location detection probability without significant sacrifice in communication performance.

VI. ACKNOWLEDGEMENT

This work was supported by the UK Engineering and Physical Sciences Research Council (EPSRC) under Grant EP/Y000315/1.

REFERENCES

- [1] T. Xu, F. Liu, C. Masouros, and I. Darwazeh, "An experimental proof of concept for integrated sensing and communications waveform design," *IEEE open J. Commun. Soc.*, vol. 3, pp. 1643–1655, Sep. 2022.
- [2] Z. He, W. Xu, H. Shen, D. W. K. Ng, Y. C. Eldar, and X. You, "Full-duplex communication for ISAC: Joint beamforming and power optimization," *IEEE J. Sel. Areas Commun.*, vol. 41, no. 9, pp. 2920–2936, Sep. 2023.

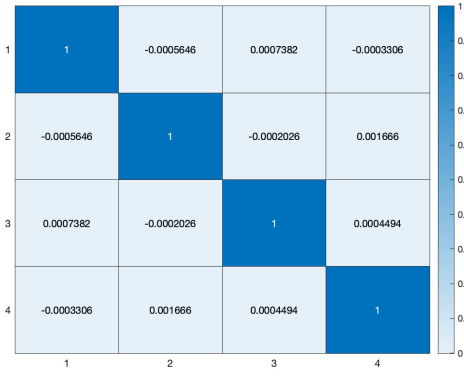


Fig. 6. The correlation heatmap of different antennas.

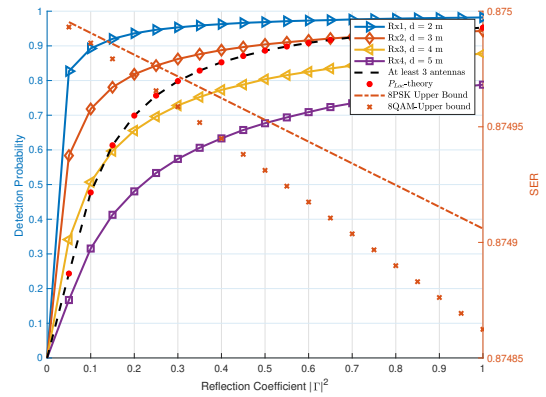


Fig. 7. Tag's detection probability versus the reflection coefficient.

- [3] Y. Zhang, F. Gao, B. Li, and Z. Han, "A robust design for ultra reliable ambient backscatter communication systems," *IEEE Internet Things J.*, vol. 6, no. 5, pp. 8989–8999, Oct. 2019.
- [4] D. T. Hoang, D. Niyato, D. I. Kim, N. V. Huynh, and S. Gong, *Ambient Backscatter Communication Networks*. Cambridge Univ. Press, Cambridge, U.K., 2020.
- [5] D. Galappaththige, C. Tellambura, and A. Maaref, "Integrated sensing and backscatter communication," *IEEE Wireless Commun. Lett.*, vol. 12, no. 12, pp. 2043–2047, Dec. 2023.
- [6] X. Wang, Z. Fei, and Q. Wu, "Integrated sensing and communication for RIS-assisted backscatter systems," *IEEE Internet Things J.*, vol. 10, no. 15, pp. 13716–13726, Aug. 2023.
- [7] A. Bekkali, S. Zou, A. Kadri, M. Crisp, and R. V. Penty, "Performance analysis of passive UHF RFID systems under cascaded fading channels and interference effects," *IEEE Trans. Wireless Commun.*, vol. 14, no. 3, pp. 1421–1433, Mar. 2015.
- [8] A. Kumar, D. Manjunath, and J. Kuri, *Communication Networking: An Analytical Approach*. San Francisco, CA: Morgan Kaufmann Publishers Inc., 2004.
- [9] B. S. Çiftler, A. Kadri, and I. Güvenç, "IoT localization for bistatic passive UHF RFID systems with 3-D radiation pattern," *IEEE Internet Things J.*, vol. 4, no. 4, pp. 905–916, Aug. 2017.
- [10] M. K. Simon, *Probability Distributions Involving Gaussian Random Variables: A Handbook for Engineers and Scientists*. Norwell, MA: Kluwer, 2002.
- [11] I. S. Gradshteyn and I. M. Ryzhik, *Table of Integrals, Series, and Products*, California: Elsevier, 7th edition, 2007.
- [12] Y. Zhang, F. Gao, L. Fan, X. Lei and G. K. Karagiannidis, "Backscatter communications over correlated Nakagami-m fading channels," *IEEE Trans. Commun.*, vol. 67, no. 2, pp.1693–1704, Feb. 2019.